Au-supported on Fe-doped ceria solids prepared in water-in-oil microemulsions: catalysts for CO oxidation

O.H. Laguna[1]*, M.A. Centeno[1], M. Boutonnet[2], J.A. Odriozola[1]

[1] *Instituto de Ciencia de Materiales de Sevilla, Centro Mixto Universidad de Sevilla-CSIC, Avenida Américo Vespucio 49, 41092 Seville – Spain*

[2] *KTH—Royal Institute of Technology, School of Chemical Science and Engineering, Department of Chemical Engineering and Technology, Stockholm, Sweden*

* Corresponding author: ohlaguna@icmse.csic.es

Abstract

Gold catalysts were synthesized by deposition-precipitation employing Fe-doped ceria systems, previously obtained by means of the water-in-oil microemulsions methodology with different iron contents (10, 25 and 50 Fe at.%). The final catalysts were tested in the CO oxidation reaction in presence of H_2. After gold deposition the crystalline structure of the supports was not altered. Moreover no XRD lines associated to gold were detected, indicating its high dispersion. Solid solution was generated in all samples, although the segregation of iron oxide was detected for the material with the highest iron loading. This phenomenon was then enhanced for the corresponding gold catalyst that also presented sintering of the gold nanoparticles.

Strong interaction between gold and the oxygen vacancies of the supports was demonstrated, as well as the promotion of the reducibility of surface Ce^{4+} and Fe^{3+} species at low temperatures. A remarkable promotion of the CO conversion at lower temperatures respect to that of the supports was observed for the gold catalysts. Below 120 ºC, lower the amount of iron incorporated, higher the catalytic performance of the catalyst. This behaviour is closely related not only to a high gold dispersion but also to the ability for creating additional oxygen vacancies in the support, required for the CO oxidation reaction.

1. Introduction

The CO oxidation is an interesting process from the technological point of view, since the conversion of such molecule into CO_2 results determinant for controlling pollution caused by emissions coming from vehicles or some industrial processes [1]. In this sense, several catalysts with variable chemical composition have been studied for carrying out such reaction, demonstrating remarkable results of CO conversion at temperatures very close or even below room temperature [1, 2].

There are also applications where the CO oxidation with O_2 must be achieved in the presence of other oxidizable molecules. This is the case of the PROX reaction, which is one of the final steps for cleaning H_2, produced from organic molecules by means of reforming processes, for been used in fuel cells [3]. For the PROX reaction, small amounts of O_2 are included in order to convert the CO to levels not exceeding 10 ppm, which is an important requirement of low temperature (< 100 ºC) polymer electrolyte membrane (LT-PEMFC) type fuel cells, because the useful life of these sort of devices for producing electricity by transforming H_2 into H_2O electrochemically, may be considerably reduced by deactivation with CO [3]. According to this, processes such as the PROX reaction require not only active catalysts able to convert as much CO as possible, but also must be selective systems able to avoid the H_2 consumption.

In the search of highly active and selective catalysts during the CO oxidation reaction, several systems have been considered [4], being the gold based ones particularly attractive because of their widely recognized ability for carrying out such reaction at very low temperatures [5]. This strongly depends on the size of the gold species [6, 7], and different works have demonstrated the capital role of supports for controlling it. For instance, ceria has been widely employed for this purpose, especially because of its structural properties which allows creating oxygen vacancies, whose are punctual defects that may act as preferential sites for the nucleation of gold controlling its dispersion [8].

A strategy to modulate the oxygen vacancies population in the ceria lattice is doping it with heteroatoms of different chemical nature than that of cerium. In this sense, Fe is an interesting candidate due to its smaller ionic radius than Ce^{4+} and Ce^{3+} cations, and also its own redox behaviour (Fe^{2+}/Fe^{3+}). On the other hand, as important as the choice of the dopant is the choice of the synthesis method. Indeed for Fe-doped ceria systems, the oxygen vacancies formation by isomorphic substitution of Ce^{4+} by Fe^{3+} cations may be altered by the interaction between these defects and iron species

located at interstitial positions in the ceria lattice [9], being this strongly related with the homogeneity of the prepared solid, and the enhancement of the Ce – Fe interaction, both properties clearly dependent of the applied synthesis procedure.

Considering the relevance of the synthesis procedure for obtaining doped ceria supports, the applying of microemulsions is a promising strategy, since it allows obtaining highly homogeneous materials with controlled structural properties and particle sizes [10]. This methodology has been employed not only for preparing metal nanoparticles but also metal oxides and mixed metal oxides for catalytic and electrochemical processes. The synthesis of inorganic nanoparticles of metal and/or metal oxides has been achieved in water-in-oil microemulsions composed by small aggregates (micelles) at the microscopic level [10]. These aggregates act as small reactors where the synthetic reactions occur, for instance, the combination of cations for obtaining the mixed oxide.

The synthesis of Fe-doped ceria systems using water-in-oil microemulsions has been recently proposed [11]. The obtained materials present a high homogeneity and intimate Fe-Ce interaction which allows the promotion of oxygen vacancies as a function of the amount of iron incorporated. Based on these interesting properties, they are adequate candidates for preparing gold catalysts.

For all above, the present work is devoted to the synthesis of gold catalysts using as supports a series of Fe-doped ceria solids with different iron contents prepared by means of water-in-oil microemulsions. The principal aim is to evaluate the influence of the modification of the ceria by the different contents of iron in the interaction of these materials with gold. On the other hand, the possible modifications of the interaction between ceria and the noble metal will be correlated with the catalytic behaviour in the CO oxidation reaction, where H_2 is included in the feed-stream in order to evaluate not only the total conversion of CO, but also the selectivity of the process.

2. Materials and methods

2.1. Synthesis of the Fe-doped ceria supports and the gold catalysts

The Fe-doped ceria systems employed in the present study as supports has been previously analyzed [11]. These were obtained by means of the water-in-oil microemulsions methodology, and according to this procedure, two microemulsions

were prepared: the first one (ME1) containing the cationic precursors of the mixed oxide [($Ce(NO_3)_3$ and $Fe(NO_3)_2$)] and the second one (ME2) containing the precipitating agent (NH_3). The formulation of both microemulsions was the same (presented in Table 1) and it has been optimized in order to ensure the transparency (optical isotropy) and stability of these colloidal systems, while the content of metallic cations and precipitating agent were maximized [12].

Three different iron contents were evaluated (10, 25 and 50 Fe at.% according to Eq 1. In all cases, a 2M concentration of metallic cations (Fe^{2+}+Ce^{3+}) in the dispersed aqueous phase of the ME1, and a 9/1 NH_3-to-(Fe+Ce) molar ratio in the dispersed aqueous phase of the ME2, was used.

$$\text{Fe at.\%} = \frac{Fe_{atoms}}{Fe_{atoms} + Ce_{atoms}} \qquad \text{(Eq 1)}$$

ME1 and ME2 were prepared separately and then ME1 was added dropwise over the ME2 under continuous stirring at room temperature. The mixture was kept under stirring during 24 h. Then the obtained precipitated was collected by centrifugation, washed five times with a 1:1 methanol/chloroform mixture and three times with methanol. The separated solid was dried at 60 ºC for 24 h and finally calcined at 500 ºC (10 ºC/min) for 2 h [11].

As for the synthesis of the gold catalysts, the deposition-precipitation method was carried out according to a previous report [13]. For that purpose the adequate amount of $HAuCl_4$ to obtain 1 Au wt.% was dissolved in distilled deionized water ($6.0x10^{-4}$ M), and the pH was fixed near to 8 with NaOH 0.1 M. This pH was employed based in other report that established this as adequate for the deposition of gold over ceria surfaces applying this procedure [14]. Then the solution was heated at 70 ºC and the Fe-doped support was added under continuous stirring for 20 min. The solid was separated from the liquid by filtration and washed several times with deionized water until Cl^- and NO_3^- disappeared. Finally, it was dried overnight at 100 ºC and finally calcined at 300 ºC for 2 h.

The obtained Fe-doped ceria solids and the gold catalysts were named as: CeFe10, CeFe25, CeFe50, and AuCeFe10, AuCeFe25, AuCeFe50, respectively.

2.2. Characterization of the obtained materials

The elemental composition of the samples was determined by X-ray fluorescence (XRF) spectrometry in a Panalytical AXIOS PW4400 sequential spectrophotometer with Rh tube as source of radiation. The measurements were performed onto pressed pellets containing 6 wt% wax.

Specific surface area was determined by the BET method using the N_2 adsorption/desorption measurements at liquid nitrogen temperature in a Micromeritics ASAP 2010 apparatus. Before analysis, the samples were degassed at 150 ºC for 2 hours under vacuum.

The XRD analyses were carried out using a Siemens® D500 diffractometer and employing the Cu Kα radiation (40 mA, 40 kV). The patterns were recorded with 0.017º step size and 275 s of step time.

The UV-Vis spectra were measured on a Varian® spectrometer model Cary 100, equipped with an integrating sphere and using $BaSO_4$ as reference. All the spectra were recorded in diffuse reflectance mode and transformed to a magnitude proportional to the extinction coefficient through the Kubelka-Munk function, $F(\alpha)$.

Raman spectra were obtained in a dispersive Horiva Jobin Yvon LabRam HR800 spectrometer, with a 20 mW He–Ne green laser (532.14 nm) operating at 5 mW. The microscope used a 50x objective and a confocal pinhole of 1000 μm.

Temperature Programmed Reduction (TPR) experiments were carried out in a U-shape quartz reactor. For every experiment 50 mg of solid were loaded and submitted to a 50 mL/min total flow of H_2 5 Vol.% in Ar, while the temperature raised at 10 °C/min from room temperature to 900 °C. A cold trap prior to the thermal conductivity detector (TCD) was used to condense the H_2O produced during the reductions processes.

2.3. Catalytic activity measurements

The catalytic tests were carried out in a fixed-bed cylindrical stainless steel reactor with internal diameter of 9 mm, inserted in a Microactivity Reference unit (PID Eng&Tech®) that allowed the control of the temperature and the composition of the feed-streams that passed through the sample. For every experiment 100 mg of solid were used

(particle size 100 < ϕ < 200 μm), and diluted with crushed glass (particle size 100 < ϕ < 200 μm), achieving a bed of about 5 mm in length. Firstly the materials were activated under a 30 mL/min total flow of 21% O_2 in N_2 at 300 ºC for 2 h. Then, a feed-stream (100 mL/min: CO 1 Vol.%, O_2 1 Vol.%, H_2 50 Vol.%, and N_2 48 Vol.%) was passed through the fixed bed at different temperatures (50-200 ºC).

Reactants and products were analysed and quantified by gas chromatography with a micro GC (Varian® CP-4900), equipped with a Porapak® Q, a Molecular Sieve 5A and two TCD detectors. The CO conversion and the selectivity to CO_2 were calculated according to Eq 2 and Eq 3, respectively. F_{in} and F_{out} refer to molar flow rates at the reactor inlet and outlet, respectively [15].

$$\text{CO conversion (\%)} = \frac{(F_{CO,in} - F_{CO,out}) \times 100}{F_{CO,in}} \qquad \text{(Eq 2)}$$

$$\text{Selectivity to } CO_2 \text{ (\%)} = \frac{(F_{CO,in} - F_{CO,out}) \times 100}{2(F_{O_2,in} - F_{O_2,out})} \qquad \text{(Eq 3)}$$

3. Results and discussion

The chemical composition and the specific surface area values of the gold catalysts are presented in Table 2. The corresponding values of the supports, previously published [11] are included also for sake of comparison.

The Fe at.% of the solids is not modified after the deposition of gold, consequently the supports and the gold catalysts exhibit a content of iron which is very close to the nominal one. As for the loading of noble metal, the intended value (1 wt.%) was achieved for the AuCeFe10 and AuCeFe25 solids. However for the AuCeFe50, the observed value is 25 % below the target. Concerning this regard, authors such as Haruta [6] or Moreau and Bond [16] has remarked that during the synthesis of gold catalyst by deposition-precipitation, the gold uptake results strongly influenced by several features of the support such as crystallinity, chemical composition, textural properties, crystallographic phase, the Z-point, and the presence of oxygen vacancies, hydroxyl groups, and other defects. Consequently, the lowest loading of gold observed in the case of AuCeFe50 may be produced by alterations in one or more of these properties.

Textural properties (BET surface area, pore volume and average pore size) of the gold catalysts are similar to those of the supports. Despite this, the solids with the highest iron loading present significantly higher specific surface areas.

The XRD patterns of the gold catalysts are presented in Figure 1, including those of the supports (previously published in [11]).

The main reflections of the gold catalysts are the same as for the supports, corresponding to *c*-CeO_2. Additionally, the shift to higher 2Θ values of these reflections with the loading of dopant agent (Fe) is maintained after the deposition of gold, confirming the solid solution formation in all cases, as was previously discussed for the supports [11]. Moreover, no modifications in the crystallite size values obtained by means of the Scherrer equation are observed for the catalysts respect to those of the supports. On the other hand, the formation of a segregated α-Fe_2O_3 phase is noticeable only for the solids with 50 Fe at.%, throughout the evolution of the signals associated to the (110) and (104) crystallographic planes, being more intense and defined for the catalyst than for the support.

Concerning the presence of gold, only the AuCeFe50 solid exhibits a reflection that may be associated to the (111) crystallographic plane of metallic Au. For the other systems no signals due to gold are detected, which may be produced by the low concentration of such noble metal in the catalysts, or to its small crystalline domain. Since this gold diffraction is observed in AuCeFe50 sample despite its lowest gold loading (Table 1), the small crystallite size of the gold nanoparticles seems to be the more plausible option. Therefore, we can consider that AuCeFe10 and AuCeFe25 catalysts must present a higher dispersion of gold than that of the AuCeFe50 sample.

Recently we have also observed the influence of other doping agents such as Zr [17], Zn [18], Eu [19], Ni, Cr [20] and Cu [13] on the achieved dispersion of gold over doped ceria, even employing Fe as doping agent but applying other synthesis procedures [9, 21]. These studies, in good agreement with other several reports presented in literature [22-26], demonstrated that parameters such as the concentration, the oxidation state, the ionic radii, the electronegativity, and the electronic properties of the dopant, determined the achieved structural modifications of the ceria lattice, which controlled the ability of the mixed system for the nucleation of gold nanoparticles.

On the other hand, as was mentioned above, other relevant feature of the XRD pattern of the AuCeFe50 is the evidence of characteristics signals of hematite, being more intense and defined for the catalyst than for the support, Figure 2.

The additional calcination at 300 ºC after the deposition of gold seems to be the main reason for the growth of the hematite phase in the case of 50 Fe at.%. Moreover, since no significant change in the crystallite size of the doped-ceria phases is observed by the presence of gold, it can be suggested that the thermal sintering affects mainly the segregated iron oxide crystals present only in the starting CeFe50 support.

The iron oxide segregation may produce the weakening of the interaction between Ce and Fe and also the interaction between the surface of the supports and the deposits of the noble metal. Indeed, the AuCeFe50 sample presents the smaller loading of gold according to XRF results (Table 2), probably because of the higher heterogeneity of the starting support. Such heterogeneity also induces the sintering of the deposits of the noble metal, making it detectable through XRD. As was discussed above, the nature of the support may influence the dispersion of the gold nanoparticles. Consequently, the lower dispersion of gold over the surface of the CeFe50 support may be produced by differences in the surface properties of this material compared with that of the other supports. Since the detected segregation of hematite in this support, the covering of the Ce-Fe mixed oxide with iron oxide may occur decreasing the interaction between such the mixed oxide and gold. Additionally the presence of Fe_2O_3 at the surface of the solid may alter properties such as the Z-point, which would be also other reason for the lower gold uptake achieved for with the CeFe50 solid.

The UV-vis diffuse reflectance spectra of the catalysts are also compared with those previously published for the supports [11] in Figure 3. In the UV region, the catalysts maintain the main three components around 218, 258 and 298 nm, commonly assigned to charge-transfer between O 2*p* and Ce 4*f* orbitals [14, 27, 28].

However in these mixed systems such region of the spectra may be complex because absorptions below 300 nm due to $O \rightarrow Fe^{3+}$ charge-transfer bands of isolated iron ions in tetrahedral and octahedral coordination may occur [29]. In addition, the contribution of the 4*f* orbitals of gold may also influence to the charge-transfer effects. Actually, the interaction between gold and the surface of the support, along with the different iron loading, may be responsible of the modifications in the intensities of such bands.

On the other hand, two signals are observed for both support and catalyst with the Fe 50 at.%. The first one centered at 382 nm, is attributed to absorptions of oligomeric clusters of α-Fe_2O_3. The other one at 528 nm (probably also presents in AuCeFe25) corresponds to *d-d* transitions ($^6A_{1g} \rightarrow {}^4T_{1g}$, and $^6A_{1g} \rightarrow {}^4T_{2g}$) in α-$Fe_2O_3$ [28]. The evidence of these signals and those centered at 472 nm for the solids with the higher Fe at.% may be associated principally to the observed segregation of hematite. This phenomenon probably is also noticed for the AuCeFe25, but in a small proportion hardly observable by XRD. Nevertheless, for the AuCeFe50 catalyst, the intensity of these signals is superior, which agrees with the sintering of the segregated hematite as discussed in the XRD analysis.

Several authors have observed modifications of the electronic environment of ceria by the inclusion of doping agents into the framework, reflected in alterations of the band gap values. The band gap may be estimated from the adsorption edge wavelength of the interband transition using the Tauc function. For insulators and semiconductors (being the second one the option of the studied materials), the square root of the Kubelka-Munk function multiplied by the photon energy is depicted versus the photon energy and extrapolating the linear zone of the rising curve to zero [30]. The obtained Tauc plots for the gold catalysts are presented in Figure 4.

In all cases (supports and catalysts) there are signals from 1.5 to 3.5 nm increasing with the content of Fe. If this is produced by the doping agent, this agrees with that discussed above about the detection of signals produced by charge-transfer with participation of the d orbitals of such transition element. This also agrees with results reported by Channei et al. [30] who observed an increase in the absorptions in the 1.5 to 3.5 eV region with the amount of iron in Fe-doped CeO_2 films with 0.5 – 5 Fe mol.%.

Besides this, the presence of gold seems to alter the Tauc plots (Figure 4). One of the probable contributions of gold species to the absorption may be ascribed to the surface plasmon resonance of metallic fine particles of such noble metal. This phenomenon is a collective oscillation of conduction electrons in response to optical excitation and it has been observed in several systems containing this metallic element, commonly in the 500-600 nm range [31, 32]. . The position and intensity of such band strongly depended on aspects such as the shape and size of the deposits of gold, and the dielectric properties of the surrounding material.

In our case, all of these parameters are being altered differently for the studied solids, as can be inferred from the structural analysis using the XRD experiments, since differences in the size of the clusters of gold, the variable amount of inserted Fe^{3+} cations into the CeO_2 lattice, or even the segregation of α-Fe_2O_3 are observed. In this sense, the surfaces of the catalysts are different from each, thus resulting in diverse electronic distributions. In addition, considering the complexity of the matrices of the catalysts composed by three metallic cations and the coexistence of different phases, the differentiation of the components that are contributing to the UV adsorption in the Tauc plots (Figure 4) is difficult.

The differences between the UV adsorption edges of the supports and the catalysts from 1.5 to 3 eV allow establishing that the interaction between gold and the surface of the catalysts is altered by the content of iron in the support as was suggested above in the discussion about the XRD results. This is consistent with that described by González Castaño et al. for gold catalysts deposited on Fe-doped CeO_2/Al_2O_3 and CeO_2/Al_2O_3 supports for the water gas shift reaction [32]. In this work it was remarked that the position of the plasmon of gold observed by UV-Vis spectroscopy depends on the presence of iron in the support. This doping agent delocalized the $4f^1$ electrons of cerium through the produced orbitals by the interaction between the two cations Ce^{4+} and Fe^{3+} [Ce(Fe)-OV_o)-Ce(Fe) orbitals], resulting in the distortion of the electronic density of gold. According to these authors, such assumption fits fairly well with the Frost's junction theory [33] that proposed the modification of the band gap structure of a semiconducting oxide and a metal with high work function. The modified band gap structure allows the electron produced by ionizing oxygen vacancies in the structure of the oxide, to be distributed between the oxide conduction band and the available Fermi levels of the metal [32].

Since the multi-component formulation of the catalysts and the contribution of different components to the UV adsorption edge making it complex, the establishment of the band gap energy values for the doped-ceria results hardly achievable. Although as a general trend we are able to say that in the gold catalysts the possible band gap energy values seem to decrease, according to the shape of the curves in Figure 4, in the 1.5 to 4 eV range, the combination of the absorptions due to the plasmon of gold, the iron species and the cerium rich phase hinders the correct layout of the straight line intersecting the X axis in the band gap value. Despite this, the decreasing of the band gap by the interaction between the surface of the supports and the nanoparticles of gold in an Au/Fe-doped ceria/Al_2O_3 catalyst is plausible according to that proposed by

González Castaño et al. [32], since gold introduces energetic levels between the valence and conduction band of the Fe doped ceria phase [34].

As for the Raman spectroscopy studies of the prepared catalysts, the corresponding spectra are presented in Figure 5.

For the AuCeFe10 and AuCeFe25 solids, no significant changes are detected respect to the supports [11], presenting in all cases the same signals ascribed to the ceria structure. The more intense band (460 cm^{-1}) is produced by the F_{2g} vibrational mode of the oxygen atoms surrounding each Ce^{4+} cation [35-37]. The other band centered at 596 cm^{-1} is due to the existence of oxygen vacancies (Ov) in the structure of the CeO_2 [35, 37]. The occurrence of these punctual defects create distortions in the framework of the ceria lattice whose may be responsible of the evolution of the Raman bands below 300 cm^{-1} (also detected for the supports [11]), which agrees with that proposed by other authors about the evidence of partial tetragonalization in ceria systems, including doped solids with different cations, by detecting similar bands [38, 39]. Nevertheless, considering that XRD patterns demonstrated the solid solution formation using 10 and 25 Fe at.%, the presence of Fe^{3+} cations into the ceria network must be also responsible of such tetragonalization, since the ionic radius of Fe^{3+} (0.78 Å) is lower than that of Ce^{4+} (0.97Å) [40]. Therefore, the signals at 186 and 257 cm^{-1} (Figure 5) do confirm the modification of the bare CeO_2 by the strong interaction with Fe as doping agent, and the presence of gold seems do not alter them remarkably.

Concerning the AuCeFe50 catalyst, its Raman spectrum is considerably different to those of the AuCeFe10 and AuCeFe25 ones, since a series of bands is observed, mostly consistent with those characteristics of a hematite structure (α-Fe_2O_3 with D_{3d}^6 crystal space group) [41-44]. The high symmetry of hematite allows seven Raman phonons below 620 cm^{-1}, and the most intense ones match those observed in the AuCeFe50 solid, Figure 5. Additionally around 460 cm^{-1} there is a broad signal that may be produced by the F_{2g} mode of the ceria structure, which is overlapped with the A_{1g} band of the hematite phase.

Despite the important evolution of the signals of hematite compared to those of the ceria structure in the AuCeFe50 catalyst, the estimation of the amount of segregated iron oxide by means of comparing the areas and/or intensities of the Raman signals is hardly achievable, since this would not be normalized. However these results confirm

the higher segregation of hematite in this catalyst after the deposition of gold observed in the XRD patterns and the UV-Vis spectra.

Other interesting feature of the Raman spectra obtained for the studied solids is not only the observable presence of the oxygen vacancies signal (Ov) in some materials (AuCeFe10 and AuCeFe25) but also the different intensities of such band, because it may be influenced not only by the interaction between Fe^{3+} and Ce^{4+}/Ce^{3+} cations in the structure of the supports but also the presence of gold in the surface of these. It must be remarked that in the case of AuCeFe50, if this Ov signal exists, it would present a low intensity compared with that of the signals due to the iron oxide, and it would be overlapped into broad signal starting from 525 cm^{-1}, becoming hardly differentiable.

In previous studies about the synthesis of doped ceria structures and applying a pseudo sol-gel procedure, using doping agents as Zr, Zn, and Fe, the oxygen vacancies signal observed in Raman Spectroscopy was also analyzed [9, 11, 17, 18]. For that purpose the Ov/F_{2g} area ratio between the areas of the oxygen vacancies and F_{2g} mode signals has been calculate, in order to establish a normalized comparison between different spectra, in such a way that the higher the Ov/F_{2g} ratio, the higher the population of oxygen vacancies. This is convenient since shape, position and intensity of the signals may be influenced not only for structural features of the materials, but also the size of the particles effect may alter these parameters [45, 46]. In this sense, the obtained Ov/F_{2g} ratios for the gold catalysts are presented in Figure 6, along with those values of the supports (previously published [11]), for sake of comparison.

For both AuCeFe10 and AuCeFe25 solids, the Ov/F_{2g} ratio (associated to the oxygen vacancies population) is lower than for the corresponding supports. Consequently the interaction between the noble metal and some of these defects over the surface of the supports is plausible. Actually the decreasing of the Ov/F_{2g} ratio in the AuCeFe25 solid is strongest than that of the AuCeFe10, respect to those of the corresponding supports, that could be associated to modifications of the particle size for the deposits of noble metal, or the electronic interaction between gold and the support, as was demonstrated in the UV-vis analysis. Despite that, although the Ov/F_{2g} ratio may be associated to the oxygen vacancies population, this is not a precise or an exact estimation of these defects and the results presented in Figure 6 have to be understood principally in qualitative terms in order to avoid speculations.

Which is remarkable is that our results agree with several reports that proposed the role of oxygen vacancies in CeO_2 as preferential sites for the nucleation of gold nanoparticles, probably controlling the size of such deposits [8, 19, 25, 47-52]. Indeed the interaction between gold and oxygen vacancies in other supports such as TiO_2 it has been observed too [48, 53]. According to this, the results presented in Figure 6 seem to be expectable. However, there are details that must be remarked. For instance although AuCeFe10 and AuCeFe25 samples present lower oxygen vacancies populations than the starting supports, it is interesting that a certain proportion of them remains on the surface, not interacting with gold and being detectable in the Raman spectra. On the other hand, the amount of such remaining oxygen vacancies in the gold catalysts follow the same trend than for the supports, being higher for the solid with the 10 Fe at.%.

On the other hand, despite it is widely accepted that oxygen vacancies prefer to be located at the surface of the oxides, which is thermodynamically enhanced by the reduction of the free Gibbs energy [54, 55], the creation of such defects into the bulk of the solids may also occur. In this sense, the remaining vacancies detected in our gold catalysts suggests two main possibilities: i) these are located at the surface and not all of them are interacting with gold clusters, or ii) the oxygen vacancies of the CeFe10 and CeFe25 are distributed not only at the surface but also into the bulk of these materials, therefore after the deposition of gold, just the surface vacancies would vanish.

Concerning the stability of oxygen vacancies in ceria, Plata et al. [56] reported a multilayer structure of CeO_2 linked to yttrium-stabilized zirconia (YSZ) for DFT calculations, and established that the required energy for the creation of an oxygen vacancy at the surface (1.72 eV) is lower than for obtaining this defect into the bulk (2.42). Similar observations about the evolution of these defects in ceria were carried out by Krcha et al. [57], applying DFT-U calculations. They remarked the difficulty for creating two consecutive vacancies in the ceria framework, being specially disadvantaged into the bulk, where the tensions of the structure are difficult to be compensated. However, they observed that the energetic barrier for the creation of new vacancies may be reduced by the inclusion of a doping agent such as Zr^{4+}. From these results it could be inferred that the expansion of the ceria lattice by the creation of a Ce^{3+} cation due to the oxygen vacancy (implying the reduction of a Ce^{4+} cation), may be compensated by a contraction effect caused by the insertion of a cation with lower ionic radius such as Zr^{4+}. Associating this case with our systems, the effect of

shrinkage of the structure is carried out by Fe^{3+} cations. Consequently a higher population of vacancies, distributed not only at the surface but also into the bulk, may be indicating a homogeneous distribution of the iron species along the extension of the CeFe10 and CeFe25 materials, which is maintained for both AuCeFe10 and AuCeFe25 catalysts. This would be a consequence of the enhanced interaction between both cerium and iron species, by means of the microemulsions methodology employed for obtaining the supports. However, despite the observed benefits of the microemulsions methodology, the 50 Fe at.% loading seems too high for obtaining an homogeneous mixed system and the segregation is detected for the support and later, more strongly for the catalyst.

Complementing the characterization of the prepared catalysts, the reducibility was also evaluated by TPR and the obtained profiles are compared in Figure 7 with those of the supports (previously published [11]).

It is difficult to differentiate specific reduction events considering the complex matrix of the materials and the strong interaction between the elements composing them. However some features of the TPR profiles may be remarked in order to analyze the observable influence over the reducibility of depositing gold on the doped systems.

The supports present three main reduction zones. The first one (< 400 ºC) was associated principally to the reduction of Fe^{3+} species into Fe^{2+} at the surface [58, 59]. Nevertheless the reduction of some Ce^{4+}, with a surface character too, must be also accounted. In the intermediate zone (400 – 700 ºC), the contribution of the reducibility of iron species seems to be more relevant because the intensity of the broad observed signals increases with the loading of Fe. The reduction of the Fe^{2+} cations into Fe^{0} occurs in this zone, although the reduction of Ce^{+4} cations is also probable. As for the CeFe50 support an additional signal appears at the beginning of this intermediate reduction zone (434 ºC), probably due to the same reduction processes ($Fe^{2+} \rightarrow Fe^{0}$ and $Ce^{4+} \rightarrow Ce^{3+}$) [58, 59], but occurring at different temperatures because of the heterogeneity of such sample produced by the segregation of hematite.

Finally, the reduction zone at higher temperatures (> 700ºC) is principally associated to the reduction of bulk Ce^{4+} species. Nevertheless in the case of the CeFe50 solid, such process may be combined with the intense contribution of the reduction of iron species into Fe^{0} inside the bulk of the segregated hematite [11], covering both the intermediate and the final zone of reduction.

Concerning the gold catalysts the first remarkable difference is the existence of a negative signal at low temperatures (100 ºC) representing not hydrogen consumption but production. Since the emission of hydrogen is not expected from the gold catalysts, this may be produced by the adsorption of such gas during the stabilization of the base line and a subsequent desorption at low temperatures just when the heating program started. Although complementary experiments would be needed to confirm the following suggestion, H_2 spillover process may be occurring between gold nanoparticles and the mixed oxides. This is plausible considering reports devoted to this regard such as that presented by Collings et al. [60] where the Surface Plasmon Spectroscopy was proposed as tool for evaluating the dissociation of hydrogen in Au nanorods embedded in different supports. These authors observed that hydrogen did not dissociate on gold nanorods at room temperature when in contact with silica. However the spillover, implying the dissociative adsorption of hydrogen, was noticed when semiconductors materials (ZnO and TiO_2), demonstrating the crucial role of the support on controlling the electronic environment of the deposits of gold, allowing the electronic transfer from the adsorbed H_2 molecules to the surface of the materials.

In our gold catalysts, probably the dissociative adsorption of hydrogen occurs at room temperature during the stabilization of the signal of the TCD prior to the heating during the TPR experiment. Then, once the temperature slightly increases, the reverse spillover would take place. This would explain the emission of hydrogen detected as negative signals in the TPR profiles of the gold catalysts. The occurrence of the H_2 spillover would corroborate the strong interaction between gold and the surface of the Fe-doped oxides demonstrated through the other applied experimental techniques. Indeed, such interaction may be involved in the occurrence of the first reduction peak observed for the gold catalyst (centered in the 200 - 225 ºC interval), because it is principally produced by the hydrogen consumption for the reduction of surface Fe^{3+} and Ce^{4+} species. However this reduction occurs at lower temperatures than for the supports, thus demonstrating the easy reduction of the surface cations enhanced by their interaction with gold probably through the occurrence of the H_2 spillover effect discussed above.

The hydrogen consumption due to the reduction of cationic species of gold should not be discarded at all, since several authors have demonstrated evidences of the existence of Au^{+} and/or Au^{3+} cations [61, 62] in similar systems. Nevertheless, considering the noble character of this metal, it is assumable that a high proportion of

this metal must be present as Au^0 in the fresh catalysts. Additionally, accounting the small amount of gold atoms respect to those of Fe and Ce in the chemical formulation of our catalysts, even assuming that all the gold species would be present in the higher oxidation state (3+), the theoretical amount of hydrogen required for their complete reduction is close to a hundred times lower than that needed for the reduction of iron and ceria in their maximum oxidation states (3+ and 4+ respectively). Consequently, the contribution of cationic species of gold could be discarded in these solids.

In an intermediate zone of the TPR of the gold catalysts (~300 – 600 ºC), there are also reduction events whose intensity increase with the iron content. These processes seem to be similar to those of the supports but shifted to lower temperatures. In the case of the AuCeFe50, this phenomenon was more notable and considering that for the corresponding support CeFe50 the reduction of some iron species were also associated to the broad peak centered at 684 ºC, the interaction between gold and the segregated iron oxide in this solid was highly probable, resulting in the shift to lower temperatures of the reduction of the segregated hematite. In this sense, the broad reduction peak centered at 488 ºC for the AuCeFe50 catalyst may be including some gold-iron oxide interactions too. In general, these results agree with the enhancement of the reducibility reported to occur by combining gold and doped-ceria systems [21, 22, 63]. Despite this, some reduction events at higher temperatures (above 600 ºC) are detected. The temperatures of such processes are similar to those of the corresponding supports (although with variable intensities) pointing to they are due to the reduction of bulk species whose reducibility is hardly modifiable by the presence of gold.

The reducibility percentage of the samples, calculated as the experimental hydrogen consumption with respect to the theoretical one, multiplied by 100, and assuming that cerium and iron are in their maximum oxidation state and are reduced to Ce^{3+} and Fe^0, discarding the small contribution possible cationic species of gold [9, 17], are presented in Table 3. The experimental hydrogen consumption is obtained by means of the integration of all the positive signals of the TPR profiles. The obtained area values are transformed to mol of H_2 using a calibration curve, previously performed for a CuO pattern. The areas of negative signals observed in the TPR profiles of the gold catalysts are not included in the estimation of the experimental hydrogen consumption.

Comparing the reducibility percentages of supports and catalysts, no major modifications are detected. Moreover, all the obtained values are similar between

them. Probably a remarkable result is the higher experimental hydrogen consumption detected for the AuCeFe50 catalyst above that of the CeFe50 support. This must be related with its higher heterogeneity and the hematite segregation, which probably implies the alteration of the amount of reducible species in the solid. However, taking into account all the assumptions considered for the calculations of the theoretical hydrogen consumption, the observed values are very similar and could be within the margin of error.

In this sense, the enhancement of the reducibility by the deposition of gold can be understood in terms of an easier reduction of the reducible species at lower temperatures, not affecting the amount of such species. The easier reduction of surface species of ceria in close contact with gold and platinum has been observed by several authors. However, recently González Castaño et al. [32] that also observed similar results in their Au and Pt catalysts deposited on Fe-doped ceria/Al_2O_3, remarked that the reduction of surface Ce^{4+} cations may be associated with the decrease of the band gap energy of the materials. Therefore, alterations in the band gap are not only produced by the inclusion of iron into the framework of ceria but also by the distortion of the electronic environment by the presence of gold on the surface, responsible also of the easier reduction of surface cationic species.

Catalytic activity measurements

The ability of the prepared catalysts for the abatement of CO in the presence of H_2 is compared with that of the supports (previously published [11]) in Figure 8.

The main result of the catalytic activity is the significant enhancement of the CO conversion of all catalysts due to the presence of gold (especially below 150 ºC). These results are consistent with several works in which the higher catalytic activity in CO oxidation reactions is achieved by means of depositing gold in reducible supports [8, 52]. Additionally in most of these works, it is remarked the relevant role of the particle size of the gold nanoparticles. Chen and Goodman [7] have demonstrated that the CO oxidation ability increases until a maximum value by decreasing the gold nanoparticles near to 3 nm, and below this size the CO conversion decreases. In our gold catalyst the particle size distribution of gold is not analyzed, and for carrying this experimental techniques such as high resolution transmission electronic microscopy (HR-TEM) are required. However, a possible effect of the particle size of the gold nanoparticles in the studied systems may be occurring.

All gold catalysts exhibit a similar catalytic activity trend. The CO conversion increases at low temperatures to a maximum and then decreases. The maximum CO conversion reached by the AuCeFe10 and AuCeFe25 catalysts is similar (~70 %) and higher than that of the AuCeFe50. Moreover, the initial conversion decreases in the following order AuCeFe10 > AuCeFe25 > AuCeFe50 that could be related with the iron content. This also agrees with the decreasing of the gold uptake, thus the lower content of gold may be also responsible of the observed results. Consequently, the differences in the catalytic activity may be consistent with the structural properties depending on the iron content and the presence of the noble metal.

For instance, the oxygen vacancies of the supports may allow modifications in the size distribution of the nanoparticles of gold, which in our case represents higher CO conversion at low temperatures as the amount of these defects increases in the catalysts. Although we cannot establish a complete size distribution of the gold nanoparticles for our catalyst, probably the interaction between oxygen vacancies and the noble metal (demonstrated above in the Raman spectroscopy studies, Figure 5) decreases the size of the nanoclusters. As higher the amount of vacancies in the support, smaller the size of the gold nanoparticles and this would be occurring in the zone when the decreasing of the species of gold results in the enhancement of the CO conversion. This would be consistent with the higher catalytic activity observed for the AuCeFe10 catalyst and then that of the AuCeFe25. Furthermore, the described phenomenon would agree with the lower activity observed for the AuCeFe50 solid, which is the material with a superior heterogeneity demonstrated by all the applied characterization techniques. Actually the oxygen vacancies population is hardly detectable for this system.

The easy reduction observed at low temperature (below 300 ºC) for the gold catalysts also agrees with the promotion the catalytic activity for the gold catalysts respect to that of the supports. Then, the easier creation of reduced Ce^{3+} in the catalysts is allowed for structures where the tolerance to the evolution of new vacancies is superior, which may be the case of the solids doped with 10 and 25 Fe at.%. These materials may compensate additional distortions in the framework of the mixed oxide for stabilizing bigger cations such as Ce^{+3}, involving also the creation of new oxygen vacancies.

Similarly to that occurring during the TPR experiments, the tolerance to the creation of additional oxygen vacancies in a reductant environment may be tested under the

reaction conditions, because of the high levels of H_2 in the feed-stream which is similar to that of the PROX reaction. Therefore, the reducibility and the evolution of these defects are closely related and strongly influence the catalytic activity in our catalysts. The electronic transfer between gold and the gaseous oxygen molecules involved in the CO oxidation is enhanced when the clusters of the noble metal are placed over oxygen vacancies as was recently demonstrated for gold catalysts using Y-doped TiO_2 as supports [48].

Concerning the selectivity to CO_2 (Figure 8B), it is maximum (100 %) for the supports at low temperatures, when the CO conversion is below 5 % and then (> 100 ºC), a strong decrease is observed, being less marked for the CeFe10 support. This represents a progressive increase of the H_2 consumption with the temperature, which is produced by the occurrence of two side reactions, in a similar way than for the PROX reactions; the H_2 oxidation and the reverse water-gas shift (R-WGS), which are enhanced with the temperature [64].

The gold catalysts do not present the maximum selectivity because, although the CO oxidation is promoted at lower temperatures, the H_2 oxidation is also enhanced, as we observed in the kinetic study during the PROX reaction of $CuOx/CeO_2$ catalyst [65]. However, the decreasing of selectivity is less strong for the catalysts than for the supports, in good agreement with the superior CO consumption not only at low temperatures but also at higher ones (Figure 8A). On the other hand, the lowest selectivity of the AuCeFe50, also demonstrates that its heterogeneity not only reduces the CO oxidation ability but also enhance the side reactions, resulting in the H_2 consumption. Consequently the materials present a high potential for been evaluated under realistic PROX conditions including not only H_2 along with CO but also H_2O and CO_2. Being especially attractive those solids with the lower iron content.

4. Conclusions

The present manuscript relies upon the successful synthesis of gold catalysts throughout the deposition-precipitation method, using Fe-doped ceria solids obtained with water-in-oil microemulsions. The starting supports presented different amounts of Fe (10, 25 and 50 at.%) and although the final catalysts present very similar gold uptakes close to the intended value (1 wt.%), the AuCeFe50 solid exhibits the lowest loading of noble metal (25% above the intended value).

Concerning the textural properties no major modifications are detected after the deposition gold. In the same way, the crystallographic phases of the catalysts with 10 and 25 Fe at.% are not modified, while for the AuCeFe50 the segregation of iron oxide (α-Fe_2O_3) was detected. This behaviour is closely related with the lowest gold uptake determined for such catalysts due to the alteration of the surface of the support by the presence of surface deposits of hematite. Additionally for this system the sintering of gold deposits occurs while for the other catalyst, the small particle size of the gold nanoparticles does not allow their detection by means of XRD.

On the other hand, the strong interaction between oxygen vacancies and gold is confirmed and the presented results demonstrated a close relation between the oxygen vacancies population and the dispersion of the noble metal. Additionally it must be remarked that despite the strong gold-oxygen vacancies interaction, not all of these vacancies are vanished after gold deposition, which is associated to especially enhanced promotion of the oxygen vacancies creation by the microemulsion method used for obtaining the Fe-doped supports. Moreover, the gold-support interaction also produces an easier reducibility of surface Ce^{4+} and Fe^{3+} cations.

Concerning the catalytic activity measurements it is remarkable the important promotion of the CO conversion at low temperatures (below 120 ºC) for the catalysts respect to that of the supports. The differences in the interaction between gold and the supports depending on the iron content also correlate with the catalytic activity performance of the studied solids, because the AuCeFe10 system with the superior catalytic activity at lower temperatures (below 120 ºC) is the material with the higher gold uptake and a superior concentration of remaining oxygen vacancies after the deposition of the noble metal, since the cooperation between gold and additional oxygen vacancies are required for activating the CO oxidation reaction.

Consequently not only the promotion of an adequate dispersion of gold nanoparticles but also the contribution of additional oxygen vacancies of the support are required in order to promote the catalytic activity during the selective CO oxidation, at low temperatures where the selectivity to the CO_2 formation is high. The needed modification of the structure of ceria for making it an enhanced support for obtaining gold catalysts seems to be one of the profits of applying microemulsion methodology, for obtaining more homogeneous solids, becoming promising catalysts for the PROX reaction.

5. Acknowledgements

The authors thank the financial support of the group TEP106 to the Junta de Andalucía.

6. References

[1] S. Liu, X. Wu, D. Weng, R. Ran, Ceria-based catalysts for soot oxidation: a review, J. Rare Earths, 33 (2015) 567-590.

[2] O.H. Laguna, L.F. Bobadilla, W.Y. Hernández, M.A. Centeno, Low-Temperature CO oxidation, in: P. Granger, V.I. Parvulescu, S. Kaliaguine, W. Prellier (Eds.) Perovskites and related mixed oxides: concepts and applications, Wiley-VCH, Weinheim, 2016, pp. 453-475.

[3] G. Chen, Q. Yuan, H. Li, S. Li, CO selective oxidation in a microchannel reactor for PEM fuel cell, Chemical Engineering Journal, 101 (2004) 101-106.

[4] N. Bion, F. Epron, M. Moreno, F. Mariño, D. Duprez, Preferential oxidation of carbon monoxide in the presence of hydrogen (PROX) over noble metals and transition metal oxides: Advantages and drawbacks, Top. Catal., 51 (2008) 76-88.

[5] M. Haruta, N. Yamada, T. Kobayashi, S. Iijima, Gold catalysts prepared by coprecipitation for low-temperature oxidation of hydrogen and of carbon monoxide, Journal of Catalysis, 115 (1989) 301-309.

[6] M. Haruta, Gold as a novel catalyst in the 21st century: Preparation, working mechanism and applications, Gold Bulletin, 37 (2004) 27-36.

[7] M.S. Chen, D.W. Goodman, Structure–activity relationships in supported Au catalysts, Catalysis Today, 111 (2006) 22-33.

[8] O.H. Laguna, M.I. Dominguez, F. Romero-Sarria, J.A. Odriozola, M.A. Centeno, Role of Oxygen Vacancies in Gold Oxidation Catalysis, in: Z. Ma, S. Dai (Eds.) Heterogeneous Gold Catalysts and Catalysis, The Royal Society of Chemistry, 2014, pp. 489-511.

[9] O.H. Laguna, F. Romero Sarria, M.A. Centeno, J.A. Odriozola, Gold supported on metal-doped ceria catalysts (M = Zr, Zn and Fe) for the preferential oxidation of CO (PROX), Journal of Catalysis, 276 (2010) 360-370.

[10] M. Boutonnet, S. Lögdberg, E. Elm Svensson, Recent developments in the application of nanoparticles prepared from w/o microemulsions in heterogeneous catalysis, Current Opinion in Colloid & Interface Science, 13 (2008) 270-286.

[11] O.H. Laguna, M.A. Centeno, M. Boutonnet, J.A. Odriozola, Fe-doped ceria solids synthesized by the microemulsion method for CO oxidation reactions, Applied Catalysis B: Environmental, 106 (2011) 621-629.

[12] S. Nassos, E.E. Svensson, M. Nilsson, M. Boutonnet, S. Järås, Microemulsion-prepared Ni catalysts supported on cerium-lanthanum oxide for the selective catalytic oxidation of ammonia in gasified biomass, Applied Catalysis B: Environmental, 64 (2006) 96-102.

[13] O.H. Laguna, W.Y. Hernández, G. Arzamendi, L.M. Gandía, M.A. Centeno, J.A. Odriozola, Gold supported on CuO_x/CeO_2 catalyst for the purification of hydrogen by the CO preferential oxidation reaction (PROX), Fuel, 118 (2014) 176-185.

[14] M.A. Centeno, C. Portales, I. Carrizosa, J.A. Odriozola, Gold supported CeO_2/Al_2O_3 catalysts for CO oxidation: influence of the ceria phase, Catal Lett, 102 (2005) 289-297.

[15] O.H. Laguna, M.I. Domínguez, S. Oraá, A. Navajas, G. Arzamendi, L.M. Gandía, M.A. Centeno, M. Montes, J.A. Odriozola, Influence of the O_2/CO ratio and the presence of H_2O and CO_2 in the feed-stream during the preferential oxidation of CO (PROX) over a CuO_x/CeO_2-coated microchannel reactor, Catalysis Today, 203 (2013) 182-187.

[16] F. Moreau, G.C. Bond, Influence of the surface area of the support on the activity of gold catalysts for CO oxidation, Catalysis Today, 122 (2007) 215-221.

[17] O.H. Laguna, A. Pérez, M.A. Centeno, J.A. Odriozola, Synergy between gold and oxygen vacancies in gold supported on Zr-doped ceria catalysts for the CO oxidation, Applied Catalysis B: Environmental, 176–177 (2015) 385-395.

[18] O.H. Laguna, M.A. Centeno, F. Romero-Sarria, J.A. Odriozola, Oxidation of CO over gold supported on Zn-modified ceria catalysts, Catalysis Today, 172 (2011) 118-123.

[19] W.Y. Hernandez, F. Romero-Sarria, M.A. Centeno, J.A. Odriozola, In Situ Characterization of the Dynamic Gold-Support Interaction over Ceria Modified Eu^{3+}. Influence of the Oxygen Vacancies on the CO Oxidation Reaction, Journal of Physical Chemistry C, 114 (2010) 10857-10865.

[20] T.R. Reina, S. Ivanova, M.A. Centeno, J.A. Odriozola, Catalytic screening of Au/CeO_2-MO_x/Al_2O_3 catalysts (M = La, Ni, Cu, Fe, Cr, Y) in the CO-PrOx reaction, International Journal of Hydrogen Energy, 40 (2015) 1782-1788.

[21] T.R. Reina, S. Ivanova, M.A. Centeno, J.A. Odriozola, Boosting the activity of a $Au/CeO_2/Al_2O_3$ catalyst for the WGS reaction, Catalysis Today, 253 (2015) 149-154.

[22] F. Vindigni, M. Manzoli, T. Tabakova, V. Idakiev, F. Boccuzzi, A. Chiorino, Gold catalysts for low temperature water-gas shift reaction: Effect of ZrO_2 addition to CeO_2 support, Appl. Catal. B-Environ., 125 (2012) 507-515.

[23] I.L. Violi, A. Zelcer, M.M. Bruno, V. Luca, G.J.A.A. Soer-Illia, Gold Nanoparticles Supported in Zirconia-Ceria Mesoporous Thin Films: A Highly Active Reusable Heterogeneous Nanocatalyst, Acs Applied Materials & Interfaces, 7 (2015) 1114-1121.

[24] P. Petrova, T. Tabakova, G. Munteanu, R. Zanella, M. Tsvetkov, L. Ilieva, Gold catalysts on Co-doped ceria for complete benzene oxidation: Relationship between reducibility and catalytic activity, Catalysis Communications, 36 (2013) 84-88.

[25] M. Nolan, Healing of oxygen vacancies on reduced surfaces of gold-doped ceria, The Journal of Chemical Physics, 130 (2009) 144702-144709.

[26] E.d.O. Jardim, S. Rico-Francés, F. Coloma, E.V. Ramos-Fernández, J. Silvestre-Albero, A. Sepúlveda-Escribano, Superior performance of gold supported on doped

CeO_2 catalysts for the preferential CO oxidation (PROX), Applied Catalysis A: General, 487 (2014) 119-129.

[27] S. Tsunekawa, T. Fukuda, A. Kasuya, Blue shift in ultraviolet absorption spectra of monodisperse CeO_{2-x} nanoparticles, Journal of Applied Physics, 87 (2000) 1318-1321.

[28] A.S. Reddy, C.Y. Chen, C.C. Chen, S.H. Chien, C.J. Lin, K.H. Lin, C.L. Chen, S.C. Chang, Synthesis and characterization of Fe/CeO_2 catalysts: Epoxidation of cyclohexene, Journal of Molecular Catalysis a-Chemical, 318 (2010) 60-67.

[29] M. Schwidder, M.S. Kumar, K. Klementiev, M.M. Pohl, A. Bruckner, W. Grunert, Selective reduction of NO with Fe-ZSM-5 catalysts of low Fe content - I. Relations between active site structure and catalytic performance, Journal of Catalysis, 231 (2005) 314-330.

[30] D. Channei, B. Inceesungvorn, N. Wetchakun, S. Ukritnukun, A. Nattestad, J. Chen, S. Phanichphant, Photocatalytic Degradation of Methyl Orange by CeO_2 and Fe-doped CeO_2 Films under Visible Light Irradiation, Scientific Reports, 4 (2014).

[31] P. Mulvaney, Surface Plasmon Spectroscopy of Nanosized Metal Particles, Langmuir, 12 (1996) 788-800.

[32] M. Gonzalez Castaño, T.R. Reina, S. Ivanova, M.A. Centeno, J.A. Odriozola, Pt vs. Au in water–gas shift reaction, J. Catal., 314 (2014) 1-9.

[33] J.C. Frost, Junction effect interactions in methanol synthesis catalysts, Nature, 334 (1988) 577-580.

[34] S. Deshpande, S. Patil, S. Kuchibhatla, S. Seal, Size dependency variation in lattice parameter and valency states in nanocrystalline cerium oxide, Applied Physics Letters, 87 (2005) 133113_133111-133113_133113.

[35] J.E. Spanier, R.D. Robinson, F. Zheng, S.W. Chan, I.P. Herman, Size-dependent properties of CeO_2-y nanoparticles as studied by Raman scattering, Phys. Rev. B, 64 (2001) 245407 (245401-245408).

[36] G.W. Graham, W.H. Weber, C.R. Peters, R. Usmen, Empirical method for determining CeO_2-particle size in catalysts by raman spectroscopy, Journal of Catalysis, 130 (1991) 310-313.

[37] W.Y. Hernández, O.H. Laguna, M.A. Centeno, J.A. Odriozola, Structural and catalytic properties of lanthanide (La, Eu, Gd) doped ceria, Journal of Solid State Chemistry, 184 (2011) 3014-3020.

[38] P. Fornasiero, G. Balducci, R. Di Monte, J. Kašpar, V. Sergo, G. Gubitosa, A. Ferrero, M. Graziani, Modification of the Redox Behaviour of CeO_2 Induced by Structural Doping with ZrO_2, Journal of Catalysis, 164 (1996) 173-183.

[39] M. Yashima, H. Arashi, M. Kakihana, M. Yoshimura, Raman-scattering study of cubic-tetragonal phase-transition in $Zr_{1-X}Ce_XO_2$ solid-solution, Journal of the American Ceramic Society, 77 (1994) 1067-1071.

[40] R.D. Shannon, Revised effective ionic-radii and systematic studies of interatomic distances in halides and chalcogenides, Acta Crystallogr. Sect. A, 32 (1976) 751-767.

[41] C. Baratto, P.P. Lottici, D. Bersani, G. Antonioli, G. Gnappi, A. Montenero, Sol-Gel Preparation of α-Fe_2O_3 Thin Films: Structural Characterization by XAFS and Raman, Journal of Sol-Gel Science and Technology, 13 (1998) 667-671.

[42] D.L.A. de Faria, S. Venâncio Silva, M.T. de Oliveira, Raman microspectroscopy of some iron oxides and oxyhydroxides, Journal of Raman Spectroscopy, 28 (1997) 873-878.

[43] T.P. Martin, R. Merlin, D.R. Huffman, M. Cardona, Resonant 2 mangnon Raman-scattering in $\alpha-Fe_2O_3$, Solid State Communications, 22 (1977) 565-567.

[44] K.F. McCarty, Inelastic light-scattering in α-Fe_2O_3 - phonon vs magnon scattering, Solid State Communications, 68 (1988) 799-802.

[45] H.Z. Bao, X. Chen, J. Fang, Z.Q. Jiang, W.X. Huang, Structure-activity relation of $Fe_{(2)}O_{(3)}$-$CeO_{(2)}$ composite catalysts in CO oxidation, Catal Lett, 125 (2008) 160-167.

[46] Z.Y. Pu, J.Q. Lu, M.F. Luo, Y.L. Me, Study of oxygen vacancies in $Ce_{0.9}Pr_{0.1}O_2$-delta solid solution by in situ x-ray diffraction and in situ Raman spectroscopy, Journal of Physical Chemistry C, 111 (2007) 18695-18702.

[47] M. Nolan, V.S. Verdugo, H. Metiu, Vacancy formation and CO adsorption on gold-doped ceria surfaces, Surface Science, 602 (2008) 2734-2742.

[48] F. Romero-Sarria, J.J. Plata, O.H. Laguna, A.M. Márquez, M.A. Centeno, J.F. Sanz, J.A. Odriozola, Surface oxygen vacancies in gold based catalysts for CO oxidation, RSC Advances, 4 (2014) 13145-13152.

[49] M. Boronat, A. Corma, Oxygen activation on gold nanoparticles: separating the influence of particle size, particle shape and support interaction, Dalton Trans., 39 (2010) 8538-8546.

[50] M. Boronat, A. Corma, Generation of defects on oxide supports by doping with metals and their role in oxygen activation, Catalysis Today, 169 (2011) 52-59.

[51] R. Burch, Gold catalysts for pure hydrogen production in the water-gas shift reaction: activity, structure and reaction mechanism, Physical Chemistry Chemical Physics, 8 (2006) 5483-5500.

[52] J. Guzman, S. Carrettin, A. Corma, Spectroscopic evidence for the supply of reactive oxygen during CO oxidation catalyzed by gold supported on nanocrystalline CeO_2, Journal of the American Chemical Society, 127 (2005) 3286-3287.

[53] E. Wahlstrom, N. Lopez, R. Schaub, P. Thostrup, A. Ronnau, C. Africh, E. Laegsgaard, J.K. Norskov, F. Besenbacher, Bonding of gold nanoclusters to oxygen vacancies on rutile TiO2(110), Phys. Rev. Lett., 90 (2003) 4.

[54] P.J. Gellings, H.J.M. Bouwmeester, Ion and mixed conducting oxides as catalysts, Catalysis Today, 12 (1992) 1-101.

[55] I. Kosacki, T. Suzuki, H.U. Anderson, P. Colomban, Raman scattering and lattice defects in nanocrystalline CeO_2 thin films, Solid State Ionics, 149 (2002) 99-105.

[56] J.J. Plata, A.M. Marquez, J.F. Sanz, Understanding the Interplay of Dopants, Interfaces, and Anionic Conductivity in Doped Ceria/Zirconia Heteroepitaxial Structures, Chem. Mat., 26 (2014) 3385-3390.

[57] M.D. Krcha, A.D. Mayernick, M.J. Janik, Periodic trends of oxygen vacancy formation and C–H bond activation over transition metal-doped CeO_2 (111) surfaces, Journal of Catalysis, 293 (2012) 103-115.

[58] S. Li, S. Krishnamoorthy, A. Li, G.D. Meitzner, E. Iglesia, Promoted Iron-Based Catalysts for the Fischer–Tropsch Synthesis: Design, Synthesis, Site Densities, and Catalytic Properties, Journal of Catalysis, 206 (2002) 202-217.

[59] S. Li, A. Li, S. Krishnamoorthy, E. Iglesia, Effects of Zn, Cu, and K promoters on the structure and on the reduction, carburization, and catalytic behavior of iron-based Fischer-Tropsch synthesis catalysts, Catal Lett, 77 (2001) 197-205.

[60] S.S.E. Collins, M. Cittadini, C. Pecharromán, A. Martucci, P. Mulvaney, Hydrogen Spillover between Single Gold Nanorods and Metal Oxide Supports: A Surface Plasmon Spectroscopy Study, ACS Nano, 9 (2015) 7846-7856.

[61] A. Karpenko, R. Leppelt, V. Plzak, R.J. Behm, The role of cationic Au^{3+} and nonionic Au^0 species in the low-temperature water–gas shift reaction on Au/CeO_2 catalysts, Journal of Catalysis, 252 (2007) 231-242.

[62] Q. Fu, H. Saltsburg, M. Flytzani-Stephanopoulos, Active nonmetallic Au and Pt species on ceria-based water-gas shift catalysts, Science, 301 (2003) 935-938.

[63] G. Avgouropoulos, M. Manzoli, F. Boccuzzi, T. Tabakova, J. Papavasiliou, T. Ioannides, V. Idakiev, Catalytic performance and characterization of Au/doped-ceria catalysts for the preferential CO oxidation reaction, Journal of Catalysis, 256 (2008) 237-247.

[64] J. Spivey, A. Egbebi, Heterogeneous catalytic synthesis of ethanol from biomass-derived syngas, Chem Soc Rev, 36 (2007) 1514 - 1528.

[65] G. Arzamendi, I. Uriz, P.M. Diéguez, O.H. Laguna, W.Y. Hernández, A. Álvarez, M.A. Centeno, J.A. Odriozola, M. Montes, L.M. Gandía, Selective CO removal over Au/CeFe and CeCu catalysts in microreactors studied through kinetic analysis and CFD simulations, Chemical Engineering Journal, 167 (2011) 588-596.

TABLES

Table 1. Formulation of the optimized microemulsions for the synthesis of Fe-doped ceria solids

Component	Role of the component in the microemulsion	Formulation of ME1 and ME2 (Wt. %)
n-octane	Continuous phase	53
Cetyl trimethyl ammonium bromide (CTAB)	Surfactant	13
1-butanol	Co-surfactant	13
Aqueous phase	Dispersed phase	21

Table 2. Chemical composition and specific surface area of the Fe-doped supports and the gold catalysts

Solid	BET area (m^2/g)	Fe at. %	Au wt.%
CeFe10	81	10.8	--
CeFe25	84	26.6	--
CeFe50	110	54.4	--
AuCeFe10	84	9.9	1.02
AuCeFe25	86	27.5	0.99
AuCeFe50	113	52.7	0.85

Table 3. Reducibility percentages of the Fe-doped supports and the gold catalysts

Solid	Reducibility percentage
CeFe10	76
CeFe25	80
CeFe50	78
AuCeFe10	79
AuCeFe25	74
AuCeFe50	87

FIGURE CAPTIONS

Figure 1. XRD pattern of the Fe-doped supports and the gold catalysts

Figure 2. Enlargement of the XRD pattern of the CeFe50 and the AuCeFe50 solids

Figure 3. UV-vis spectra of the Fe-doped supports and the gold catalysts

Figure 4. Tauc plots of the Fe-doped supports and gold catalysts

Figure 5. Raman spectra of the gold catalysts

Figure 6. Ov/F_{2g} area ratio for the Fe-doped supports and the gold catalysts

Figure 7. TPR profiles of the Fe-doped supports and the gold catalysts

Figure 8. Catalytic activity of the Fe-doped supports and the gold catalysts: A) CO conversion; B) Selectivity to CO conversion

Figure 1

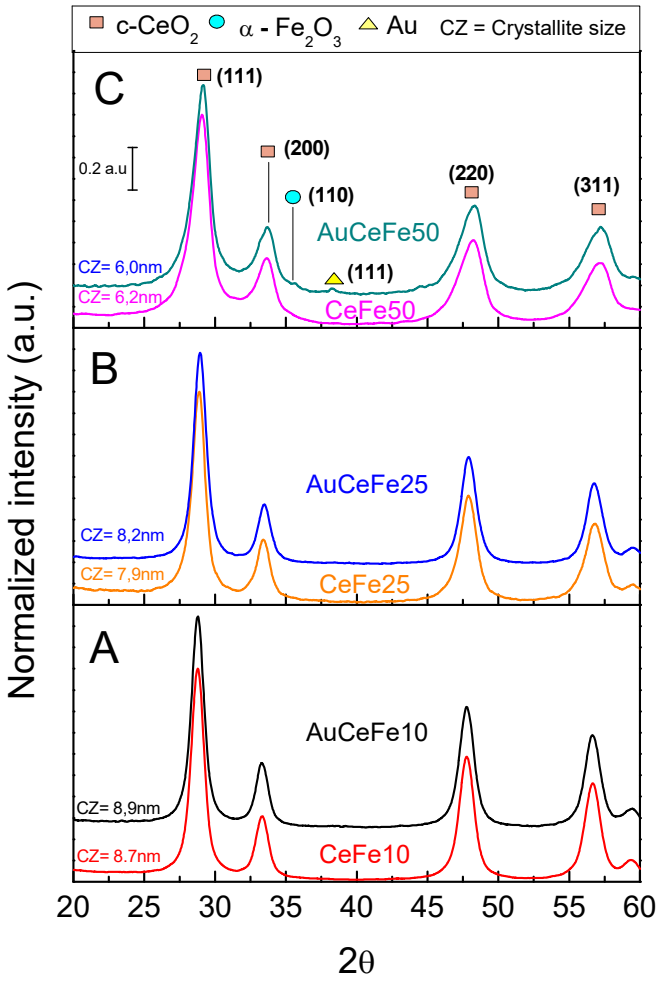
c-CeO2
α - Fe2O3
Au
CZ = Crystallite size
C
(111)
(200)
(110)
(220)
(311)
0.2 a.u
AuCeFe50
CZ= 6,0nm
(111)
CZ= 6,2nm
CeFe50
B
AuCeFe25
CZ= 8,2nm
CZ= 7,9nm
CeFe25
A
AuCeFe10
CZ= 8,9nm
CZ= 8.7nm
CeFe10
Normalized intensity (a.u.)
20
25
30
35
40
45
50
55
60
2θ

Figure 2

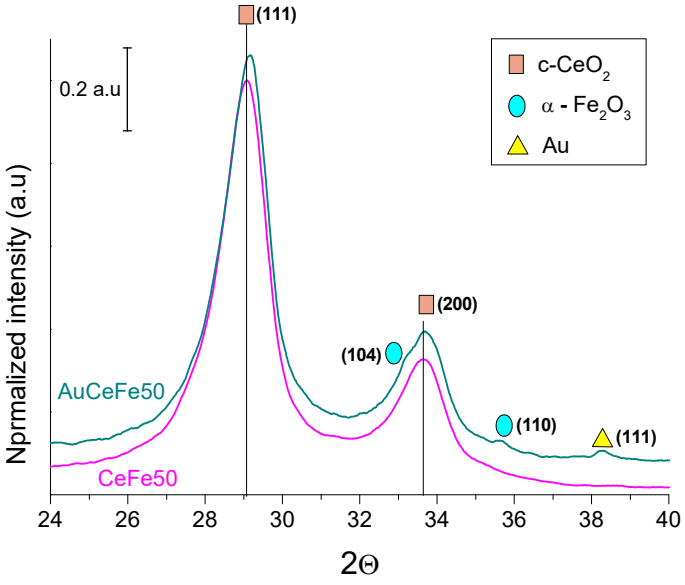
(111)
0.2 a.u
c-CeO2
α - Fe2O3
Au
(200)
(104)
(110)
(111)
AuCeFe50
CeFe50
Nprmalized intensity (a.u)
24
26
28
30
32
34
36
38
40
2Θ

Figure 3

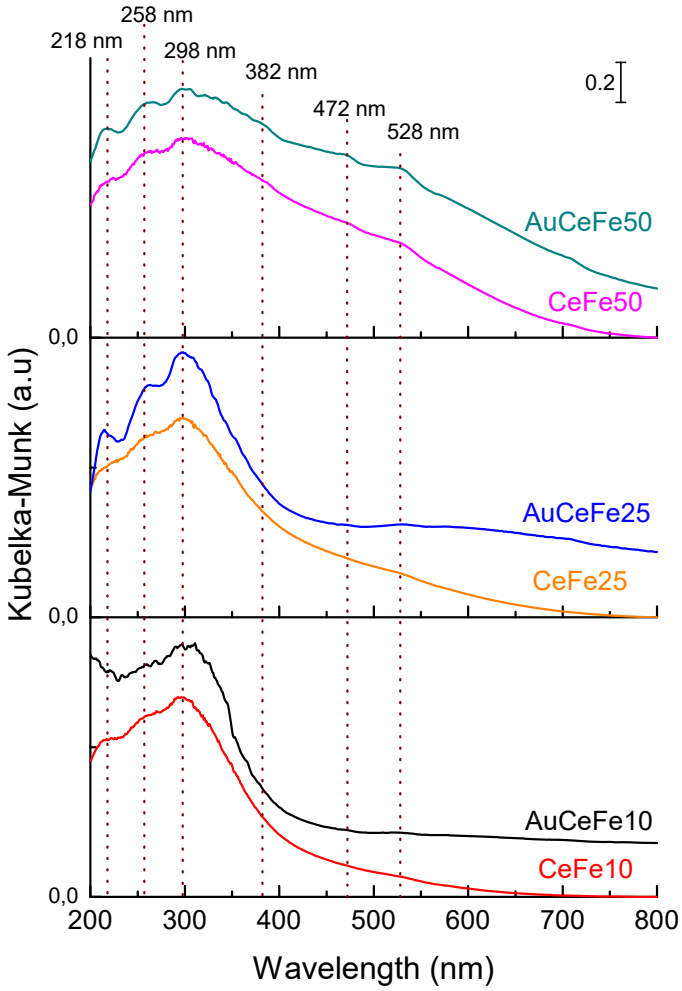
258 nm
218 nm
298 nm
382 nm
472 nm
528 nm
0.2
AuCeFe50
CeFe50
AuCeFe25
CeFe25
AuCeFe10
CeFe10
0,0
0,0
0,0
Kubelka-Munk (a.u)
200
300
400
500
600
700
800
Wavelength (nm)

Figure 4

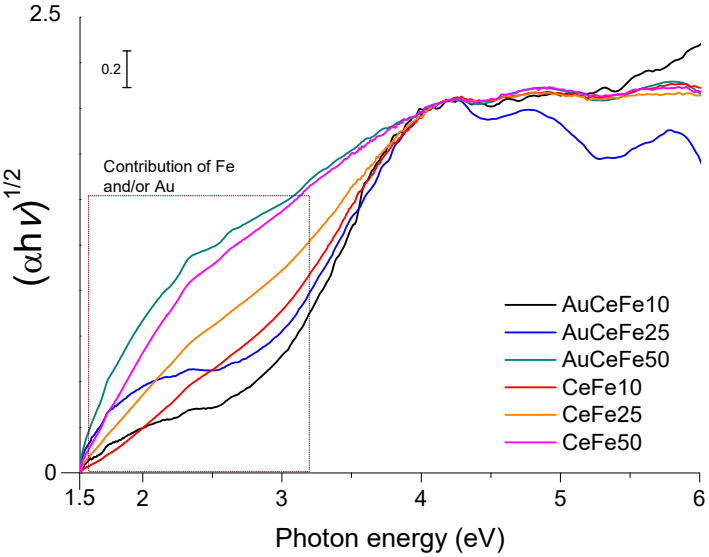
2.5
0.2
Contribution of Fe
and/or Au
$(\alpha h\nu)^{1/2}$
0
1.5
2
3
4
5
6
Photon energy (eV)
AuCeFe10
AuCeFe25
AuCeFe50
CeFe10
CeFe25
CeFe50

Figure 5

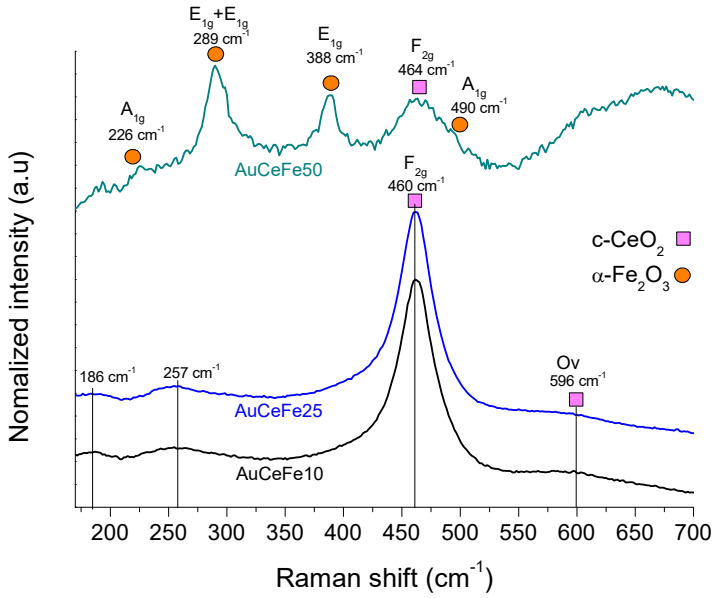
E1g+E1g
289 cm-1
E1g
388 cm-1
F2g
464 cm-1
A1g
490 cm-1
A1g
226 cm-1
AuCeFe50
F2g
460 cm-1
c-CeO2
α-Fe2O3
186 cm-1
257 cm-1
Ov
596 cm-1
AuCeFe25
AuCeFe10
Nomalized intensity (a.u)
200 250 300 350 400 450 500 550 600 650 700
Raman shift (cm-1)

Figure 6

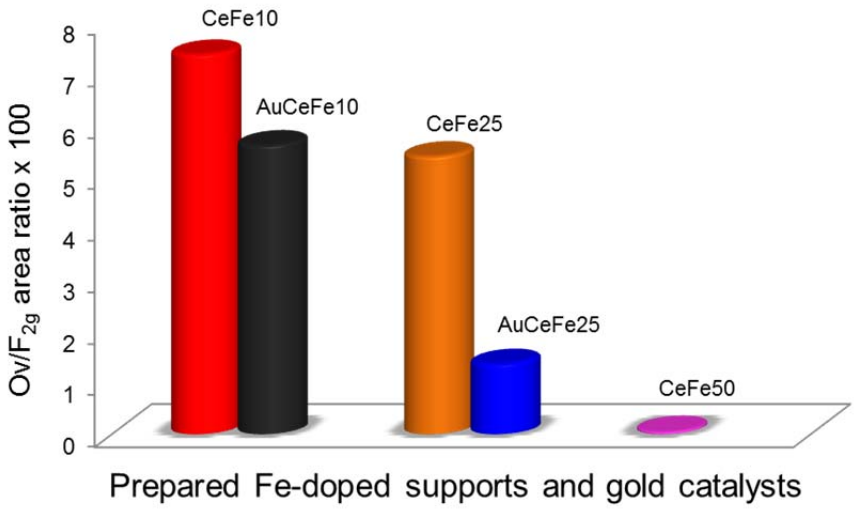
CeFe10
AuCeFe10
CeFe25
AuCeFe25
CeFe50
Ov/F2g area ratio x 100
0
1
2
3
4
5
6
7
8
Prepared Fe-doped supports and gold catalysts

Figure 7

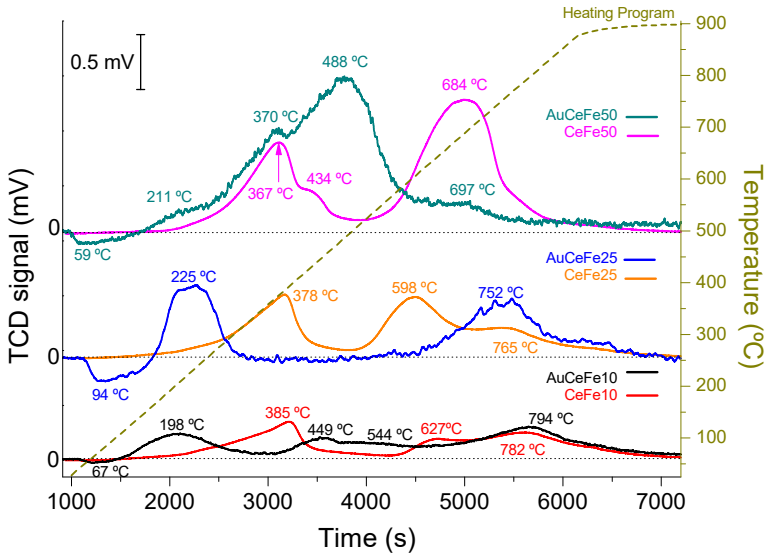
Heating Program
0.5 mV
488 ºC
684 ºC
370 ºC
AuCeFe50
CeFe50
434 ºC
211 ºC
367 ºC
697 ºC
59 ºC
AuCeFe25
CeFe25
225 ºC
378 ºC
598 ºC
752 ºC
765 ºC
AuCeFe10
CeFe10
94 ºC
198 ºC
385 ºC
449 ºC
544 ºC
627ºC
794 ºC
782 ºC
67 ºC
TCD signal (mV)
Temperature (ºC)
Time (s)
0
0
0
900
800
700
600
500
400
300
200
100
1000
2000
3000
4000
5000
6000
7000

Figure 8

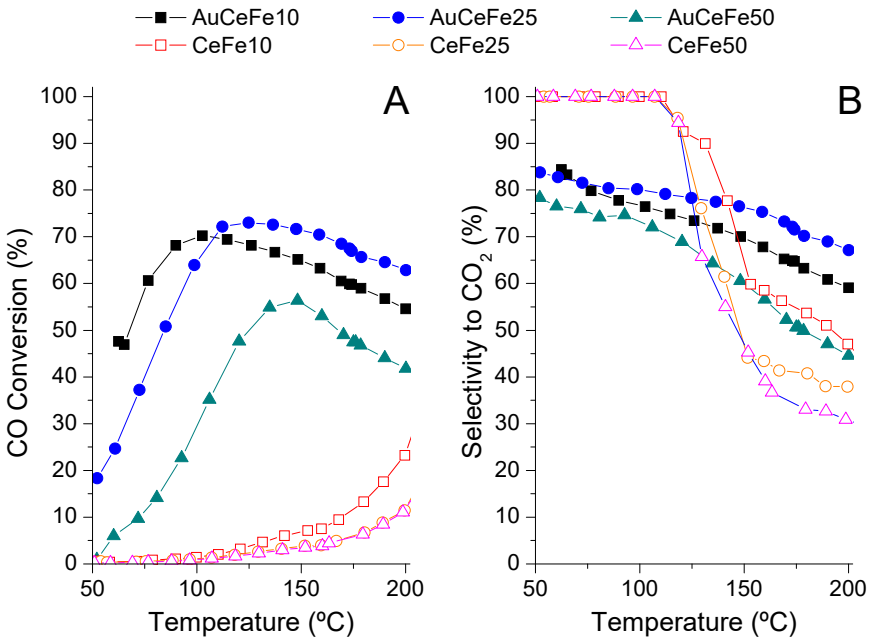
AuCeFe10
AuCeFe25
AuCeFe50
CeFe10
CeFe25
CeFe50
A
B
CO Conversion (%)
Selectivity to CO2 (%)
Temperature (ºC)
Temperature (ºC)
0
10
20
30
40
50
60
70
80
90
100
50
100
150
200